Volumetric estimates of seismic reflector rotation and convergence—tools for mapping rotation about faults and seismic stratigraphy

Satinder Chopra, Arcis Seismic Solutions, Calgary, Canada
Kurt J. Marfurt, University of Oklahoma, Norman, USA

Geometric attributes such as coherence and curvature are commonly used for mapping structural deformation and depositional environment. Coherence proves useful for identification of faults, channel edges, reef edges, and collapse features while curvature images folds, flexures, subseismic conjugate faults that appear as drag or as folds adjacent to faults, rollover anticlines, diagenetically altered fractures, karst, and differential compaction over channels. Unfortunately, these two attributes have limited value in imaging classic seismic stratigraphy features such as progradation and erosional truncation. Seismic stratigraphy refers to the analysis of the configuration and termination of seismic reflection events, packages of which are then interpreted as stratigraphic patterns. These packages are then correlated to well-known patterns such as toplap, onlap, downlap, hummocky clinoforms, and so forth, which in turn represent architectural elements of a depositional environment (Mitchum et al., 1977). By integrating these elements with well control as well as modern and paleo analogs, the interpreter produces a probability map of lithofacies. Seismic facies also thicken and thin with increasing and decreasing accommodation space. Rotation of lithologic units about faults can provide increased accommodation space or subject uplifted areas to erosion.

In this study, we review the success of current geometric attribute usage and discuss the applications of the relatively new volumetric attributes—*reflector convergence* and *reflector rotation* about the normal to the reflector dip. While the former attribute is useful in the interpretation of angular unconformities, the latter quantifies the rotation of fault blocks across discontinuities such as wrench faults. Even though the interpretational use of these two attributes is quite different, algorithmically they are tightly linked. "Reflector convergence" is a measure of the change in reflector normal about a more or less horizontal axis while "reflector rotation" is a measure of the change in reflector normal about a more or less vertical axis. Such attributes can facilitate and quantify the use of seismic stratigraphic workflows to large 3D seismic volumes.

Attribute application for stratigraphic analysis

Because of the distinct change in reflector dip and/or terminations, erosional unconformities and in particular angular unconformities are relatively easy to recognize on vertical seismic sections. Although low-coherence anomalies often appear on time slices where reflectors of conflicting dip intersect, these anomalies take considerable skill to interpret. Barnes (2000) introduced an attribute that maps such unconformities volumetrically by computing the mean and standard deviation of the vector dip within local windows. Stratigraphic facies exhibiting parallelism have a small

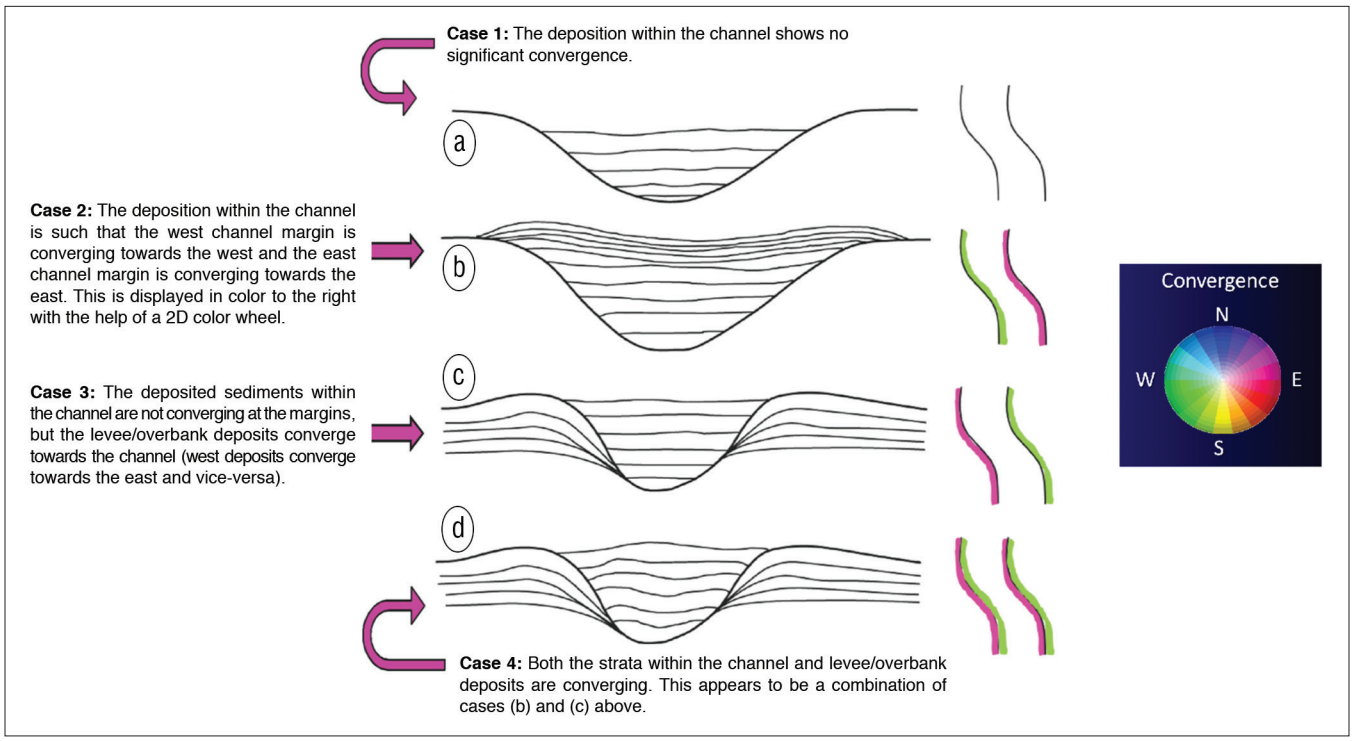

Figure 1. *Sketches demonstrating convergence within a channel with or without levee/overbank deposits. (Interpretation courtesy of Supratik Sarkar.)*

standard deviation, facies that pinch out may have a moderate standard deviation and facies that are chaotic often have a high standard deviation.

Computing a vertical derivative of apparent dip along a user-defined azimuth, Barnes (2000) also computed the convergence and divergence of reflections. In 2D, converging reflectors exhibit a decrease in dip p with depth ($dp/dx < 0$) while diverging reflectors exhibit an increase in p with depth ($dp/dx > 0$). Masaferro et al. (2003) presented a practical workflow to map progradations in 3D. They first picked a basal reflector, then flattened the data about it, and finally computed volumetric dip and azimuth. The dip and azimuth about the flattened horizon was a direct measurement of the magnitude and azimuth of downlapping (converging) reflectors against it. Van Hoek et al. (2010) discuss an attribute that may be similar to the one we present, which they describe as "a measure of the density of the flow of the dip field per unit area at any point."

Marfurt and Rich (2010) built upon Barnes' (2000) method by volumetrically computing the curl, Ψ, of the unit length vector perpendicular to the reflector, or unit normal, $\hat{\mathbf{n}}$:

$$\boldsymbol{\psi} = \nabla \times \hat{\mathbf{n}} = \hat{\mathbf{x}}\left(\frac{\partial n_y}{\partial z} - \frac{\partial n_z}{\partial y}\right) + \hat{\mathbf{y}}\left(\frac{\partial n_z}{\partial x} - \frac{\partial n_x}{\partial z}\right) + \hat{\mathbf{z}}\left(\frac{\partial n_x}{\partial y} - \frac{\partial n_y}{\partial x}\right) \quad (1)$$

where the unit normal vector has three components, n_x, n_y, and n_z and the circumflex indicates the unit normals along the x, y, and z axes.

Components of this curl vector perpendicular to the average (usually close to vertical) reflector normal, $\overline{\mathbf{n}}$, measure reflector convergence North and East components, or alternatively reflector convergence azimuth and magnitude:

$$\mathbf{c} = \overline{\mathbf{n}} \times \boldsymbol{\psi}. \quad (2)$$

Compressive deformation and wrench faulting cause the fault blocks to rotate (Kim et al., 2004). Such rotation has been observed in scale model laboratory measurements. The extent of rotation depends on the size, the comprising lithology and the stress level. Natural fractures form to compensate for the changes in space caused by fault block rotation. Fault block rotation can also control depositional processes by providing increased accommodation space in subsiding areas and exacerbating erosional processes in uplifted areas. Marfurt

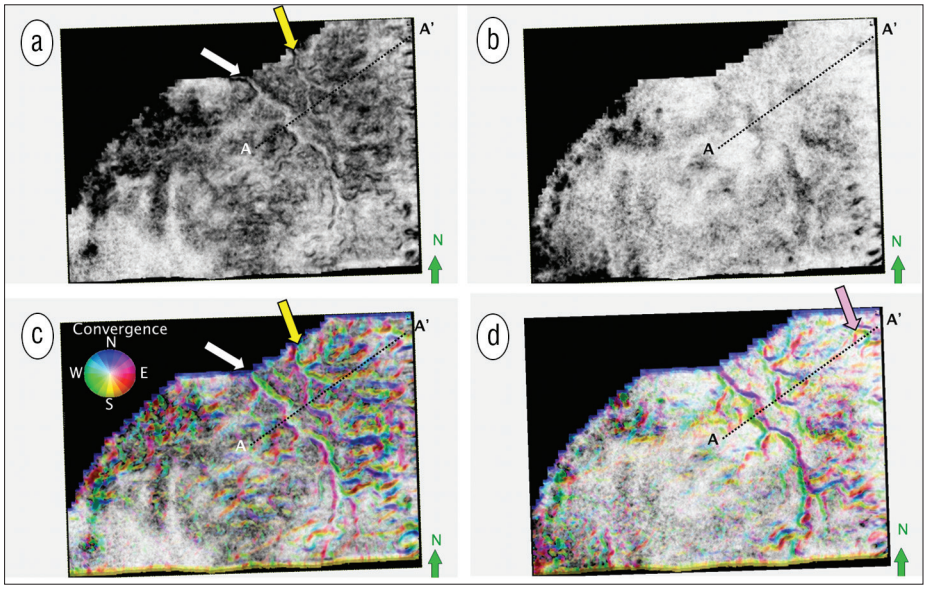

Figure 2. *Time slices through a coherence volume at (a)* t = *2.700 s and (b)* t = *2.670 showing two-channel system. The channel is clearly delineated (white and yellow arrows) in the deeper slice (a) but not at the shallower slice (b). The same two time slices at (c)* t = *2.700 s and (d)* t = *2.670 now corendered with reflector convergence. Using the sketches in Figure 1, note the change in convergence toward the center of the channel within the deeper slice show in (c) and away from the center of the channel in the shallower section seen in (d). The pink arrow in (d) indicates a buildup not seen in the corresponding coherence image in (b).*

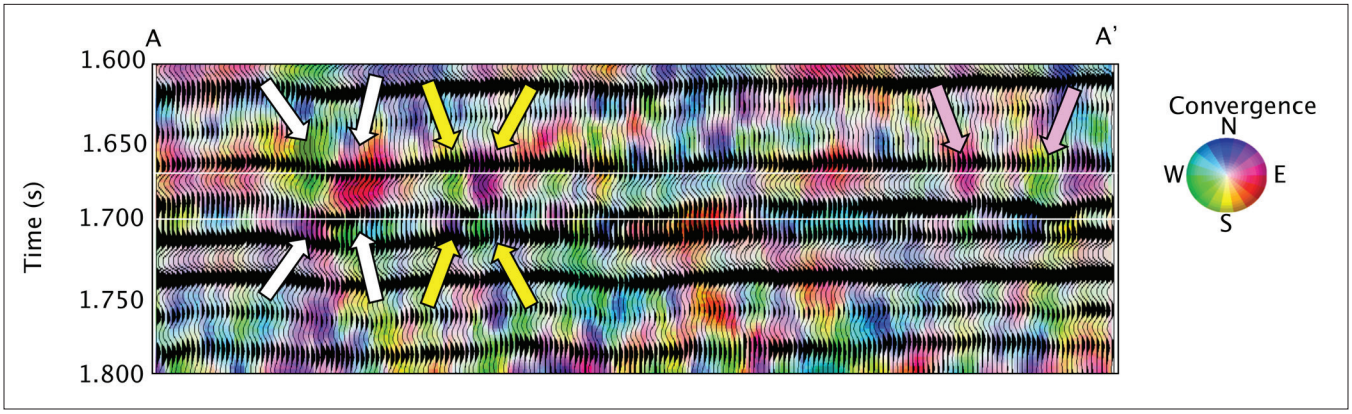

Figure 3. *Line AA' through the seismic amplitude corendered with reflector convergence. The location of line AA' is shown in Figure 2. White time lines indicate the level of the two time slices shown in Figure 2. White and yellow arrows indicate convergence anomalies associated with the westernmost and easternmost channels. Note the flip in the direction of the convergence anomalies between the incisement seen at t = 1.700 s and the differential compaction seen at t = 1.670 s. Pink arrows indicate the near-circular buildup seen in Figure 2.*

and Rich used the component of the same vector curl discussed above parallel to the average (again, usually close to vertical) reflector normal to measure reflector rotation about the normal. Such reflector rotation measures are sensitive to the type of discontinuities seen about a wrench fault and are given by

$$r = \overline{\mathbf{n}} \cdot \boldsymbol{\psi}. \quad (3)$$

Examples

Figure 1 illustrates seismic stratigraphic patterns or "reflector convergence" within a channel with and without levee/overbank deposits.

- Case 1: The deposition within the channel shows no significant convergence.

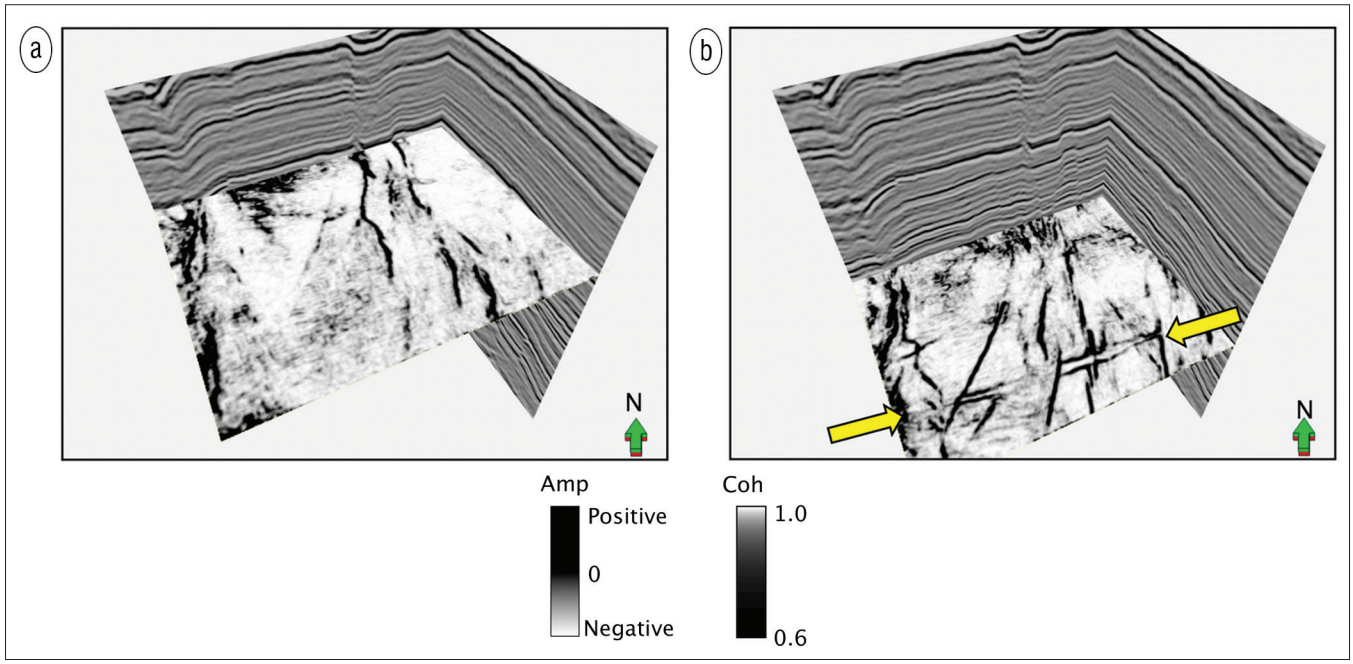

Figure 4. *Vertical slices through a seismic amplitude volume and two time slices through the corresponding coherence volume at (a)* t *=1.330 s and (b)* t *= 1.600 s showing a suite of horsts and grabens. The fault block indicated by the yellow arrows will be discussed in Figure 7. (Data courtesy of Arcis.)*

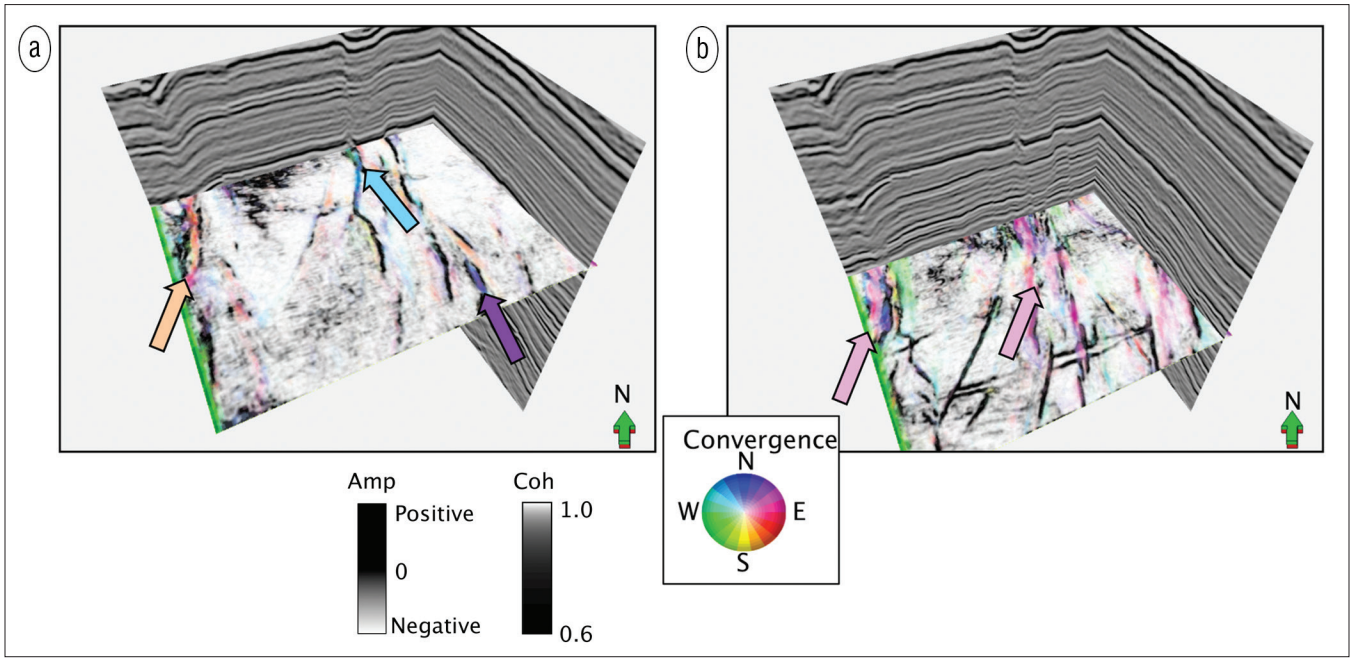

Figure 5. *The same image as Figure 4 but now with coherence corendered with reflector convergence using opacity. (a) For the time slice at* I *= 1.330 s, sediments in the graben indicated by the orange arrow are thinning to the SE, sediments indicated by the cyan arrow to the NW, and those by the purple arrow to the NNE. All three areas show thickening and thinning parallel to the graben edges. In the time slice at (b) t = 1.600 s, the sediments indicated by the magenta arrows are thinning toward the NE, more perpendicular to the graben edges. Reflectors that are nearly parallel (low-convergence magnitude) appear as white and are rendered transparent.*

WORLDWIDE LEADER IN MARINE SOURCE CONTROLLER AND RGPS TRACKING TECHNOLOGY

GunLink 4000

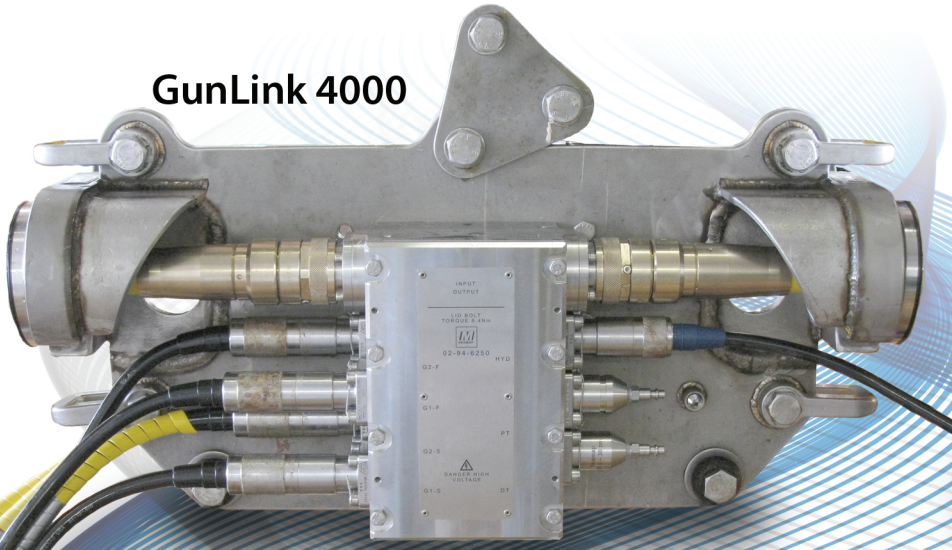

BuoyLink 4DX

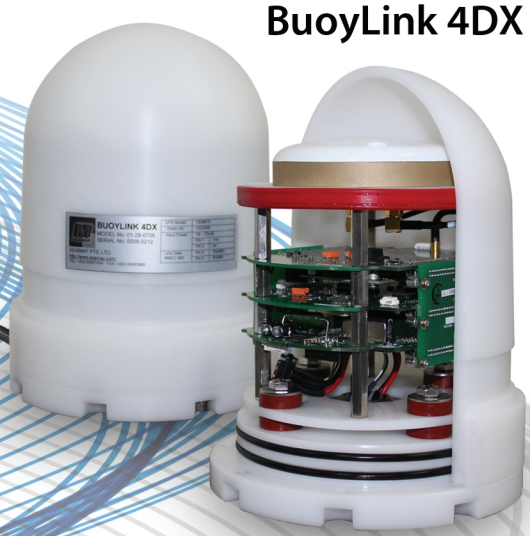

OFFSHORE TECHNOLGY SOLUTIONS™

Singapore - Shepton Mallet, UK - Huntsville, Texas

www.seamap.com

- Case 2: The deposition within the channel is such that the west channel margin is converging toward the west and the east channel margin is converging toward the east. This is displayed in color to the right with the help of a 2D color wheel.
- Case 3: The deposited sediments within the channel are not converging at the margins, but the levee/overbank deposits converge toward the channel (west deposits converge toward the east and vice-versa.
- Case 4: Both the strata within the channel and levee/overbank deposits are converging. This appears to be a combination of cases 2 and 3 above.

Notice how the convergence shows up in color (using the 2D color wheel) as displayed to the right in green and magenta colors along the channel edges.

We carried out the computation of reflector convergence and the rotation about the normal to the reflector dip attributes for a suite of

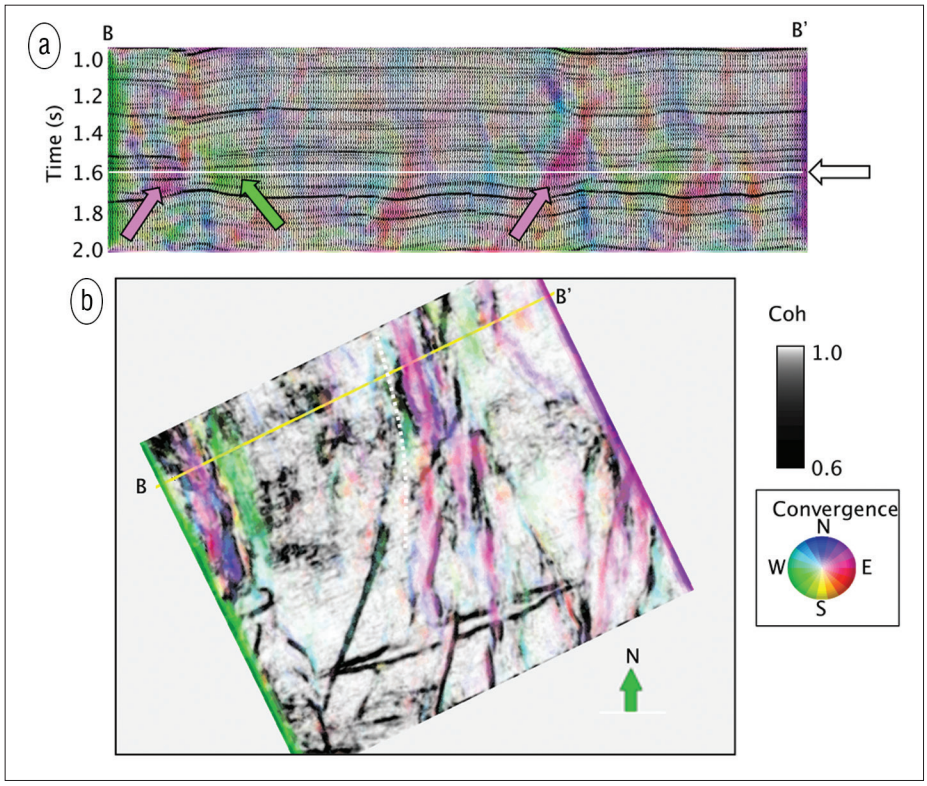

Figure 6. *(a) Vertical slice BB' through reflector convergence corendered with the seismic amplitude in a wiggle trace format. (b) A time slice at* t = *1.600 s though coherence corendered with reflector convergence. The magenta anomalies seen on the time slice correlate to the convergence of the reflectors to the NE indicated by the magenta arrows on the vertical slice. Similarly, the convergence to the SW indicated on the time slice correlates with the convergence to the SW seen on the vertical slice.*

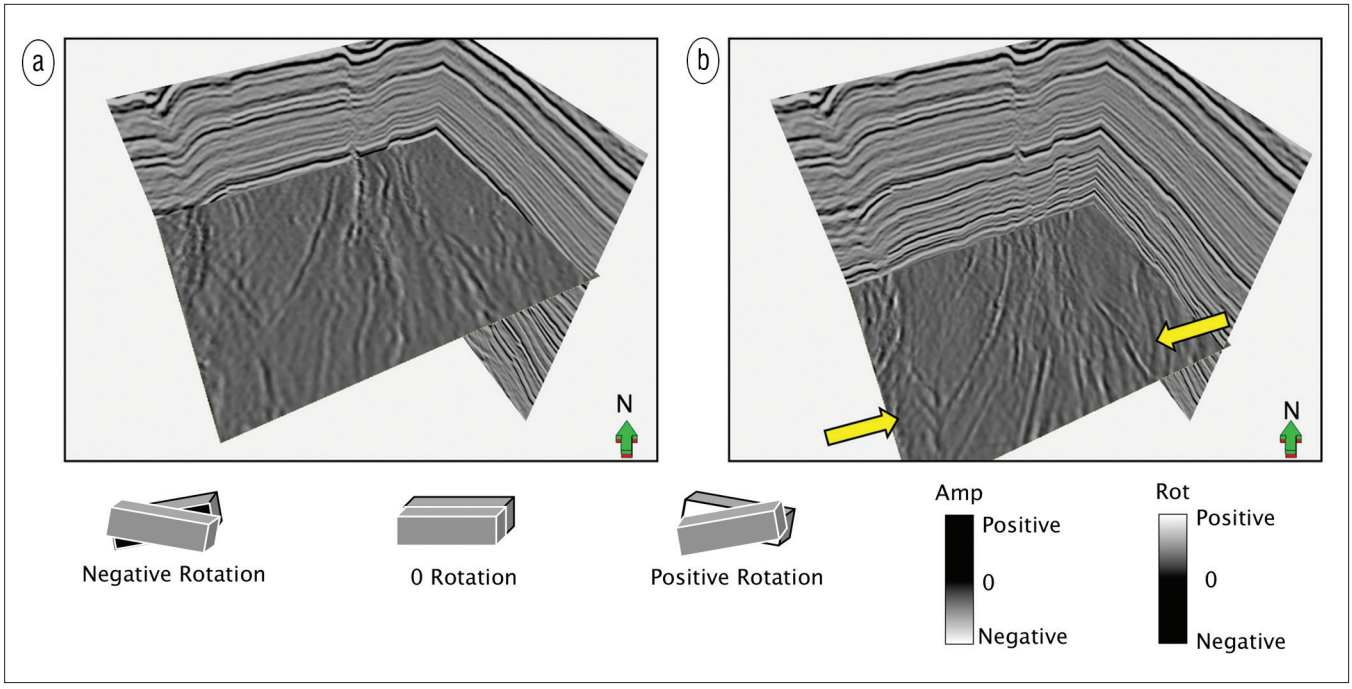

Figure 7. *The same vertical slices through a seismic amplitude volume shown in Figure 6, but now with two time slices through the corresponding volume of rotation about the average normal at (a) t = 1.330 s and (b) t = 1.600 s. Positive rotation is defined as down to the right when looking across a fault and plotted as white. Negative rotation is defined as down to the left and plotted as black. Absence of rotation is plotted as gray. This attribute delineates not only faults but also the connecting relay ramps. Rotation may give rise to increased accommodation space in the grabens or erosion of the horsts.*

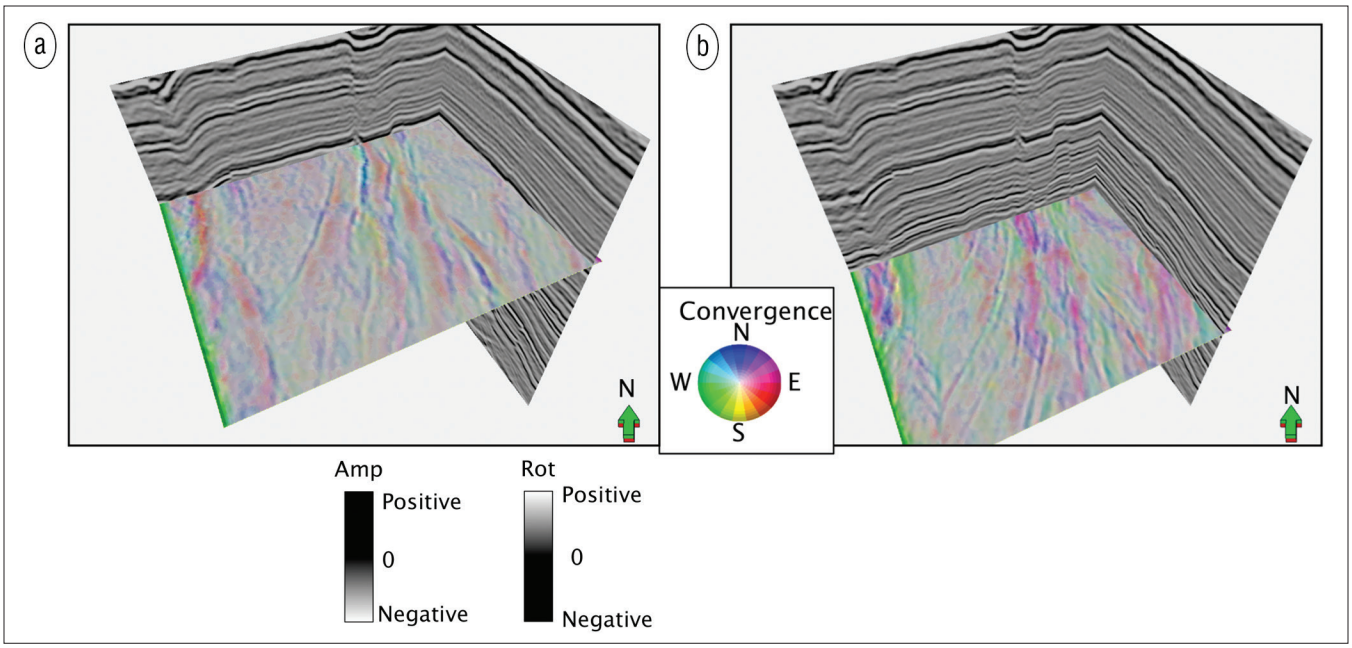

Figure 8. *The same two times as Figure 7, but now with reflector convergence corendered on the time slices using 50% transparency. Magenta indicates reflectors pinching out to the NE, orange to the SE, and green to the SW.*

3D seismic volumes from Alberta, Canada. Figure 2a and Figure 2b depict time slices through and 30 ms above an incised channel. Figure 2c and Figure 2d show the same time slices, but now corendered with reflector convergence displayed using a 2D color wheel. Figure 3 shows an arbitrary line AA' that cuts across a channel and in the shallower section across a circular buildup in the NE corner of the survey (magenta arrow). In Figure 1, we note the change in reflector convergence toward the channel axis at the level of incisement, but away from the channel axis 30 ms above. The buildup at t = 1.700 s gives rise to reflector convergence toward the buildup at the shallower level of t = 1.670 s.

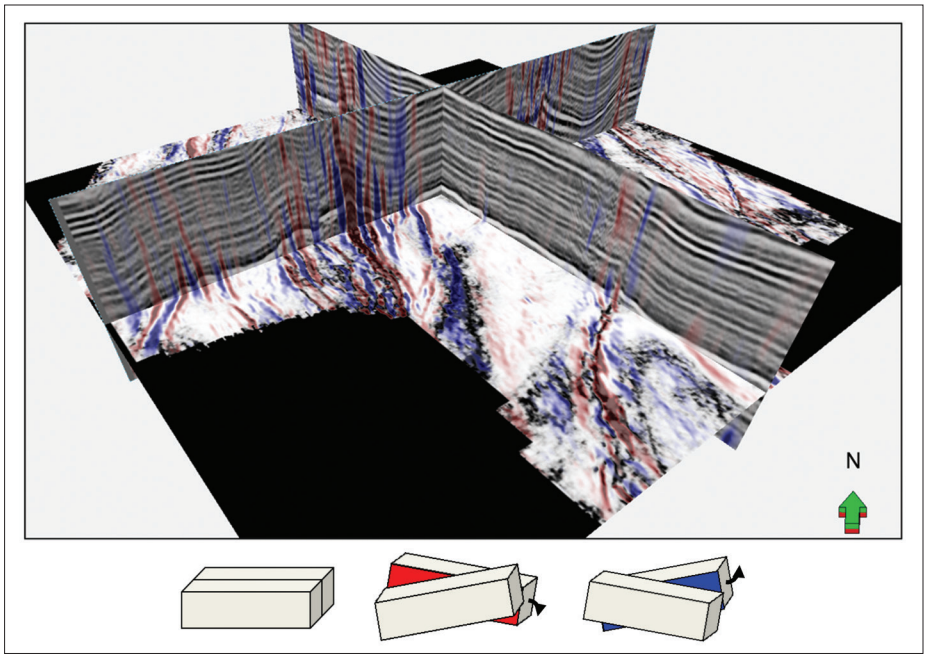

Figure 9. *Time slice at 1.190 s from the coherence volume and vertical slices through seismic amplitude corendered with vector rotation. Red indicates down to the right across the fault, while blue indicates up the right across the fault. (Data courtesy of Arcis.)*

Figure 4 is a 3D chair display with the vertical inline and crossline displays and time slices at t = 1.330 and t = 1.600 s through a coherence volume showing several lineaments corresponding to faults associated with a network of horsts and grabens. In Figure 5, these images are corendered with reflector convergence where parallel reflectors (areas with low reflector convergence) have been rendered transparent. Note that while of most of the time slices show parallel reflectors and appear like the previous image, several grabens are "color-coded', indicating that we have sediments converging to the SE (in orange), NW (in cyan), and NE (in magenta). Such reflector thinning is most easily explained by a rotation of the graben as it dropped, giving rise to increased accommodation space in a given direction. Figure 6 shows this effect using a vertical slice through seismic amplitude corendered with reflector convergence. On this slice at t =1.600 s, the grabens have rotated to the SW, such that the reflectors converge to the NE (indicated by the magenta arrows). Another graben has rotated toward the NE, with reflectors converging to the SW (indicated by the green arrow).

Figure 7 shows the results of using Equation 3 to compute the rotation about the average normal at the same two time

slices. Here we define positive rotation as down to the right across the fault (displayed in white) and negative rotation as up to the right across the fault (displayed in black). Notice the horst and graben features show considerable contrast and can be conveniently interpreted. Note the fault block indicated by the yellow arrows in Figure 4 is not seen by the rotation attribute. Many faults appear to be more continuous on rotation, particularly where the reflector offset across the fault approaches the limits of seismic resolution. Figure 8 corenders the reflector about the normal with reflector convergence displayed against a 2D color wheel using 50% transparency. As with the images with coherence in Figure 5, rotation about the faults give rise to thickening and thinning within the grabens.

Figure 9 shows rotation corendered with seismic amplitude and coherence from another survey from Alberta. Red indicates positive rotation down to the right across the fault while blue indicates negative rotation up to the right across the fault. Reflector rotation measures shear strain while curvature measures longitudinal or bending components of strain. Strain contributes significantly to the generation of natural fractures.

Conclusions

Attribute images based on the curl of reflector dip are mathematically independent but interpretationally complementary to more conventional coherence and curvature images, providing tools that quantify well-established features used in seismic stratigraphy. Application of reflector convergence to a channel system from Alberta, Canada, highlights subtle levee/overbank deposits, quantifying not only the direction but also the lateral change in thickness of the sedimentary column. Reflector convergence applied to horst and graben terrain imaged by a different survey in Alberta shows the direction and lateral change in thickness indicated increased accommodation space within down-dropped, rotated grabens. The degree and polarity (up-to-right or down-to-the right) about the near-vertical faults is measured by the reflector rotation about the normal attribute. Mathematically, curvature measures are insensitive to rotation. Together, curvature and rotation more fully quantify the strain experienced by potential reservoirs.

Although these attributes aid in mapping angular unconformities in addition to toplap and downlap configurations that form an important component in seismic stratigraphy, reflector convergence does not delineate disconformities and nonconformities exhibiting near-parallel reflector patterns. Condensed sections are often seen as stratigraphically parallel low-coherence anomalies on vertical sections. More promising solutions to mapping these features are based on changes in spectral magnitude components (Smythe et al., 2004) or in spectral phase components (Castro de Matos et al., 2011). TLE

References

Barnes, A. E., 2000, Attributes for automated seismic facies analysis: 70th Annual International Meeting, SEG, Expanded Abstracts, 553–556, http://dx.doi.org/10.1190/1.1816121.

Castro de Matos, M., O. Davogustto, K. Zhang, and K. J. Marfurt, 2011, Detecting stratigraphic discontinuities using time-frequency seismic phase residues: Geophysics, **76**, no. 2, P1–P10, http://dx.doi.org/10.1190/1.3528758.

Kim, Y. S., D. C. P. Peacock, and D. J. Sanderson, 2004, Fault damage zones: Journal of Structural Geology, **26**, no. 3, 503–517, http://dx.doi.org/10.1016/j.jsg.2003.08.002.

Marfurt, K. J. and J. Rich, 2010, Beyond curvature–volumetric estimates of reflector rotation and convergence, 80th Annual International Meeting, SEG, Expanded Abstracts, 1467–1472, http://dx.doi.org/10.1190/1.3513118.

Masaferro, J. L., R. Bourne, and J.-C. Jauffred, 2003, 3D visualization of carbonate reservoirs: The Leading Edge, **22**, no. 1, 19–25, http://dx.doi.org/10.1190/1.1542751.

Mitchum, R. M. Jr., P. R. Vail, and J. B. Sangree, 1977, Seismic stratigraphy and global changes of sea level: part 6. Stratigraphic interpretation of seismic reflection patterns in depositional sequences: section 2, in C. E. Payton, ed., Seismic stratigraphy: Application to hydrocarbon exploration: AAPG Memoir 26, 117–133.

Smythe, J., A. Gersztenkorn, B. Radovich, C.-F. Li, and C. Liner, 2004, SPICE: Layered Gulf of Mexico shelf framework from spectral imaging: The Leading Edge, **23**, 921–926. http://dx.doi.org/10.1190/1.1803504.

Van Hoek, T., S. Gesbert, and J. Pickens, 2010, Geometric attributes for seismic stratigraphic interpretation: The Leading Edge, **29**, no. 9, 1056–1065, http://dx.doi.org/10.1190/1.3485766.

Acknowledgments: We thank Arcis Seismic Solutions for permission to show the data examples as well as for the permission to publish this work.

Corresponding author: SChopra@arcis.com